Scaffolds for Tissue Engineering

DOI: 10.1002/ange.201403794

Three-Dimensional Scaffolds of Carbonized Polyacrylonitrile for Bone Tissue Regeneration**

Seungmi Ryu, Choonghyeon Lee, Jooyeon Park, Jun Seop Lee, Seokyung Kang, Young Deok Seo, Jyongsik Jang, and Byung-Soo Kim**

Abstract: *Carbon-based materials have been extensively studied for stem cell culture. However, difficulties associated with engineering pure carbon materials into 3D scaffolds have hampered applications in tissue engineering and regenerative medicine. Carbonized polyacrylonitrile (cPAN) could be a promising alternative, as cPAN is a highly ordered carbon isomorph that resembles the graphitic structure and can be easily processed into 3D scaffolds. Despite the notable features of cPAN, application of cPAN in tissue engineering and regenerative medicine have not been explored. This study, for the first time, demonstrates the fabrication of microporous 3D scaffolds of cPAN and excellent osteoinductivity of cPAN, suggesting utility of 3D cPAN scaffolds as synthetic bone graft materials. The combination of excellent processability and unique bioactive properties of cPAN may lead to future applications in orthopedic regenerative medicine.*

The sp^2-hybridized graphitic structure in one-dimensional nanotubes endows carbon nanotubes (CNTs) with unique physicochemical properties that promote osteogenic differentiation of mesenchymal stem cells (MSCs).[1,2] Despite tremendous interest in applying CNTs for bone tissue regeneration, CNTs possess a major drawback as implantable scaffolds or synthetic bone grafts.[3] In tissue engineering and regenerative medicine, scaffolds are typically required to have a three-dimensional (3D) structure to provide a surface as well as space for cell adhesion, migration, and tissue formation.[3,4] However, owing to the nanoscale nature of CNTs, manufacturing macrostructured 3D scaffolds of pure CNTs is impractical. Heat-treated polyacrylonitrile (PAN) has been proposed as an alternative to CNTs in the development of carbonaceous substances for a variety of applications, such as electrochemical sensors,[5] photocatalysts,[6] and energy storage devices.[7] After heat treatment, PAN has a graphitic structure similar to CNTs. The carbonization of PAN results in the highest carbon yield compared to other precursors without changing its basic structure.[8] Notably, its morphology and dimensions can be easily optimized during fabrication.[9] As-prepared 3D structures of carbonized PAN (cPAN) with micro-scale graphitic surfaces exhibit high surface-to-volume ratios as well as interconnected pores, both of which are preferred properties for tissue engineering scaffolds.[10]

The biological properties of cPAN for tissue engineering and regenerative medicine have not yet been explored. Herein, we hypothesize that 3D scaffolds of cPAN, which is chemically similar to CNTs, would induce MSCs to undergo osteogenesis in a similar manner to CNTs. The π-electron clouds have been reported to aid in extracellular matrix (ECM) protein adsorption (for example, fibronectin) with minimal conformational change, which facilitates cell adhesion to CNTs.[11] MSCs cultured on CNTs exhibited robust cell spreading and well-organized cytoskeletal fibers, eventually promoting osteogenic differentiation owing to the tension imposed on the cytoskeleton.[11–15] Based on these reports, we postulated that cPAN could also promote osteogenic differentiation of MSCs and that 3D scaffolds of cPAN would be suitable for use as scaffolds for bone tissue regeneration, overcoming the limitations faced by CNTs.

The fabrication of cPAN samples is shown in Figure 1 A. Electrospun PAN mats were prepared by electrospinning onto quartz plates. After carbonization of PAN mats at 800 °C under argon flow,[5,16] 2D mats of cPAN were produced. These 2D mats were used for in vitro analyses. Meanwhile, for in vivo analyses, PAN fibers were formed by electrospinning onto a petri dish containing water, and the PAN/water was lyophilized for 48 h. Generally, electrospinning allows limited control over the pore sizes, which can hinder efficient cellular ingrowth.[17] In our approach, performing the lyophilization step prior to the carbonization process overcomes this limitation by creating micro-sized pores between the electrospun PAN fibers. During the lyophilization of PAN/water, phase separation of solid fibers occurs during the ice formation, forcing the fibers to accumulate between the growing ice crystals.[18,19] After lyophilization of PAN/water mixtures, cotton ball-like 3D scaffolds of PAN fibers were obtained. The scaffolds were carbonized under 800 °C in

[*] S. Ryu,[+] Prof. B.-S. Kim
Interdisciplinary Program for Bioengineering
Seoul National University, Seoul 151-744 (Korea)
E-mail: byungskim@snu.ac.kr
J. Park, S. Kang, Prof. B.-S. Kim
School of Chemical and Biological Engineering
Seoul National University, Seoul 151-744 (Korea)
C. Lee,[+] J. S. Lee, Y. D. Seo, Prof. J. Jang
World Class University Program of Chemical Convergence for Energy & Environment, School of Chemical and Biological Engineering, Seoul National University
Seoul 151-742 (Korea)
E-mail: jsjang@plaza.snu.ac.kr
[+] These authors contributed equally to this work.

[**] This research was supported by a NRF grant (2013036054) through the National Research Foundation of Korea funded by the Ministry of Education, Science, and Technology as well as Korea Health 21 R&D Project (HI12C0199) funded by the Ministry of Health and Welfare, Republic of Korea.

Supporting information for this article is available on the WWW under http://dx.doi.org/10.1002/anie.201403794.

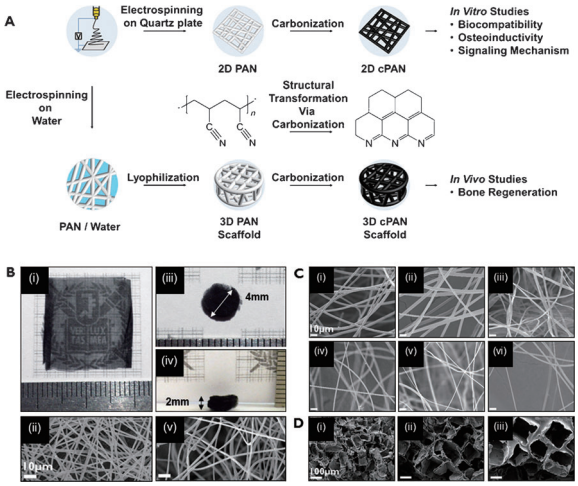

Figure 1. Preparation and characterization of cPAN scaffolds. A) Illustration of the fabrication process of cPAN scaffolds. B) i) Digital photographs of 2D cPAN mats, ii) SEM images of 2D cPAN mats, iii), iv) digital photographs of 3D cPAN scaffolds from (iii) top view and (iv) side view, v) SEM images of 3D cPAN scaffolds. C) SEM images of pore size-controlled 3D cPAN scaffolds produced by varying the weight percentage of PAN in water: i) 1, ii) 0.75, iii) 0.5, iv) 0.25, v) 0.1, and vi) 0.05 wt%. D) SEM images of cPAN scaffolds with different pore sizes: i) 50–100 μm, ii) 100–200 μm, and iii) 200–300 μm, fabricated by the solvent-casting/salt-leaching method.

argon atmosphere and then further modified into a 3D cylindrical geometry.

Figure 1 B shows electrospun cPAN fibers in 2D mats and 3D structures. The 2D cPAN electrospun mats were prepared in 2 cm by 2 cm size and were used to investigate the bioactive features of cPAN in comparison to CNT monolayers. Lyophilized cPAN scaffolds with 3D architectures (4 mm in diameter, 2 mm in height) were fabricated to examine their utility as synthetic bone graft materials in vivo. SEM images of 3D cPAN after carbonization demonstrated that average fiber diameter of electrospun cPAN remained intact. Furthermore, the pore diameter was obtained in the range of 75 μm to 100 μm. The 3D cPAN scaffolds were characterized in terms of compressive modulus, surface area, and porosity (Supporting Information, Table S1).

Figure 1 C shows SEM images of 3D cPAN scaffolds with controlled pore size. The pore size in the scaffolds was controlled by lyophilization of PAN/water solutions with different weight percentages of PAN, those ranged from 0.05 to 1 wt%. The obtained pore diameters ranged from several micrometers to hundreds of micrometers. We were able to obtain effective pore sizes of 75–100 μm at a PAN weight percentage of 0.25–0.5 wt%. According to previous reports, an effective pore size for bone growth is 75–100 μm for MSCs, as this pore size provides an environment for efficient MSC attachment, as well as a localized microenvironmental signal to direct cell behavior.[20,21] Additionally, to demonstrate facile manipulation of cPAN, sponge-type scaffolds of cPAN were prepared by the solvent-casting/salt-leaching method (SCSL) and then carbonized. The pore size of these cPAN scaffolds was easily controlled by controlling the salt size (Figure 1 D), highlighting the processability of cPAN.

C1s XPS and Raman, FTIR, and XRD analyses (Supporting Information, Figures S1–S3) demonstrated that the carbon atoms on the surface and inside of the PAN fiber re-organized into partially graphitic domains during carbonization, and the π–π transition of p-orbitals was established.[22] The elemental composition measurement (Supporting Information, Table S2) revealed that elemental percentage of carbon increased from 81.1% to 88.2%, whereas the nitrogen percentage decreased from 14.8% to 7.5%. These characterization studies showed that the carbonization process of PAN resulted in a chemical structure for cPAN that resembles that of CNT (for a detailed description, see the Supporting Information).

To investigate the biocompatibility of cPAN, human bone marrow-derived MSCs were cultured on glass, CNT, and cPAN substrates, and the viability, proliferation, and apoptotic activity of the MSCs were compared. Live/dead cell staining revealed that most of the cells on cPAN substrates were alive at days 1, 3, and 5 (Figure 2 A). Furthermore, proliferating cell nuclear antigen (PCNA) staining demonstrated enhanced proliferation in MSCs cultured on CNT compared to the cells cultured on glass (Figure 2 B). This result is consistent with previous studies, in which cells exhibited faster cellular proliferation on CNTs owing to extensive adsorption of ECM proteins on the substrates.[11,23] We examined the adsorption of fibronectin on glass, CNT, and cPAN substrates after 24 hours of incubation in serum-

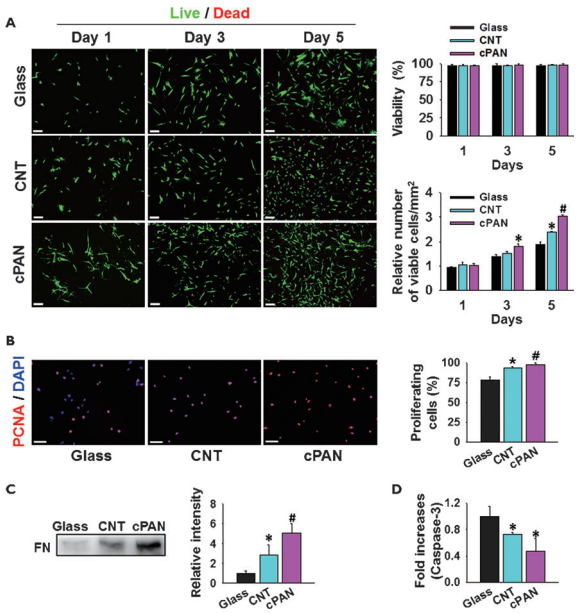

Figure 2. Biocompatibility of cPAN evaluated in terms of viability, proliferation, and apoptotic activity of MSCs cultured on cPAN substrate in vitro. A) Viability and growth of MSCs. Scale bars: 200 μm. The viable cell number was expressed relative to the number of viable cells on the glass substrate at day 1. B) Proliferating cells (red) at day 5. Nuclei were counter-stained with DAPI (blue). Scale bars: 100 μm. The ratio of PCNA-positive cells to DAPI-positive cells was quantified from the PCNA immunostaining images. C) FN adsorption on each substrate and quantification. Each band represents fibronectin adsorbed on identical area (2×2 cm). D) Apoptosis of MSCs determined based on mRNA expression of a pro-apoptotic factor, caspase-3. In (A)–(D), $n=3$, $^{*}P<0.05$ versus glass. $^{\#}P<0.05$ versus either glass or CNT.

containing culture medium by western blot analysis and observed more extensive adsorption of fibronectin on CNT and cPAN substrates than on glass (Figure 2C; Supporting Information, Figure S4). We also observed the adsorption of fibronectin protein on the substrates with FITC-labeled fibronectin (Supporting Information, Figure S5), and the results showed consistent tendency with the western blot analysis (Figure 2C). High affinity of fibronectin for CNTs was previously reported, and attributed to the graphitic structure of CNTs.[14,24] Interestingly, cPAN showed more extensive adsorption of fibronectin compared to CNT, which may explain the better performance of cPAN as a biocompatible substrate compared to glass, and even CNT, in terms of the numbers of viable cells and proliferating cells (Figure 2A and Figure 2B). Furthermore, we examined gene expression of caspase-3, a pro-apoptotic enzyme that is activated during programmed cell death. MSCs on CNT and cPAN showed lower expression of caspase-3 compared to cells on glass (Figure 2C). Collectively, our data on cell viability, proliferation, and apoptosis indicate that cPAN would be a suitable substrate for MSC culture.

Next, we tested our hypothesis that cPAN can serve as an osteoinductive biomaterial without the aid of exogenous osteogenic chemicals. First, we visualized the morphology of MSCs on each substrate (Figure 3A), as the lineage commitment of stem cells has been reported to be linked to their morphological changes.[25] On glass substrates, MSCs showed typical thin actin filaments that were arranged in parallel. In contrast, MSCs on CNT showed thicker, criss-crossed actin fibers on the cell boundaries, which was consistent with results from previous studies.[13] MSCs on cPAN also exhibited bolder, intersecting actin filaments, but with much more protruded subcellular curvatures compared to the MSCs on CNT. These morphological changes were previously reported as distinctive features of MSCs undergoing osteogenic differentiation.[14,26,27] Along with cell morphology, we examined alkaline phosphatase (ALP) activity, runt-related transcription factor 2 (Runx2) protein expression, and calcium content of MSCs on each substrate after 17 days of culture (Figure 3B–D). Upregulation of ALP activity is the quintessential event occurring during the early phase of osteogenesis.[27] Runx2 is the most specific osteoblast-associated transcription factor, controlling osteoblast commitment, differentiation, and matrix mineralization. Inorganic calcium deposition is a common characteristic of cellular bone formation.[28,29] The highest ALP activity, Runx2 expression, and calcium contents were observed in MSCs cultured on cPAN. We also examined the expression levels of the osteogenesis associated genes, such as ALP, type 1 collagen (Col 1), Runx2, osteocalcin (OC), and osteopontin (OP), in MSCs cultured for 2 and 3 weeks (Figure 3E; Supporting Information, Figure S6). Col 1 is a major ECM protein in bone; OC and OP are osteoblast-specific markers for bone matrix mineralization. Notably, the expression levels of the osteogenic markers were elevated in MSCs cultured on cPAN and CNT, with overall higher values measured for MSCs cultured on cPAN after 3 weeks. Together, these results clearly indicate that cPAN can act as an osteoinductive substrate in the absence of any osteogenic differentiation-inducing chemicals.

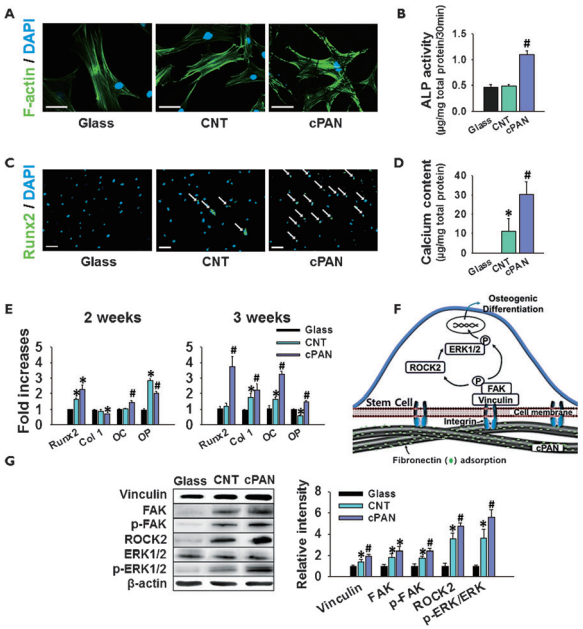

Figure 3. Osteoinductivity of cPAN and the underlying mechanisms for osteogenic differentiation of MSCs on cPAN. A) Actin cytoskeletal arrangements in MSCs. The actin filaments were stained with phalloidin (green), and cell nuclei were stained with DAPI (blue). Scale bars: 50 μm. B) Alkaline phosphatase activity in MSCs. C) Immunocytochemical staining for Runx2 (green) in MSCs. Nuclei were counterstained with DAPI (blue). The arrows indicate Runx2-positive cells (green blue). The scale bars indicate 100 μm. D) Deposited calcium in MSCs. E) mRNA expression of osteogenic markers (ALP, Runx2, type 1 collagen, osteocalcin, and osteopontin) in MSCs. F) The transduction signaling pathway for osteogenic differentiation driven by integrin–fibronectin binding. Fibronectin promotes the activation or expression of focal adhesion proteins (that is, FAK and vinculin), which subsequently triggers intracellular signaling regulation molecules such as ROCK2 and ERK1/2. Activation of these intracellular signaling molecules further leads to ostegenic differentiation of MSCs. G) Protein expression levels of molecules involved in the signal transduction pathway in MSCs. In (B), (D), (E), and (G) $n=3$, $^{*}P<0.05$ versus glass, $^{\#}P<0.05$ versus either glass or CNT.

A possible explanation for the enhanced osteogenesis of MSCs on cPAN is the enhanced adsorption of ECM proteins, which may lead to the stimulation of osteogenesis signaling pathway in the cells (Figure 3F). It was previously reported that fibronectin plays a crucial role in MSC-CNT interactions,[11] and that actin filament clustering occurs when cellular integrins bind to fibronectin.[30] The clustering of actin filaments and subsequent cytoskeletal remodeling in MSCs are promoted by the activation of focal adhesion proteins, such as vinculin and focal adhesion kinase (FAK), which are ultimately proportional to the number of integrin–fibronectin bonds.[31–33] Enhanced focal adhesion formation triggers extracellular signal-regulated kinase (ERK) signaling by ERK phosphorylation, which promotes osteogenic differentiation.[34] Additionally, activation of FAK is known to turn on Rho-associated coiled-coil protein kinase (ROCK), resulting in increased cytoskeletal tension in a positive feedback manner. The ROCK pathway eventually promotes osteogenic differentiation by activating ERK signaling.[14,25,35] cPAN exhibited adsorption of a higher amount of fibronectin

compared to CNT (Figure 2C), which might be responsible for the higher osteoinductivity of cPAN.

To confirm the mechanisms behind the enhanced osteogenic differentiation on cPAN substrates, we assessed whether the transduction signaling was elevated in MSCs cultured on cPAN compared to MSCs on glass and CNT. Western blot analysis showed that vinculin, FAK, phosphorylated FAK (that is, the activated form of FAK), and ROCK2 protein expression were the highest on cPAN (Figure 3G). It can be inferred that FAK signaling was upregulated in MSCs cultured on cPAN, which resulted in enhanced FAK autophosphorylation. Subsequently, MSCs on cPAN showed the highest phosphorylation of ERK1/2. Taken together, cPAN stimulates the upregulation of mechanotransduction signaling via the FAK-ERK pathway, which most likely contributed to the enhanced osteogenic differentiation of MSCs on the cPAN substrates.

Finally, we examined the in vivo performance of osteoinductive 3D cPAN scaffolds as synthetic bone grafts by implanting cPAN scaffolds into critical-sized calvarial defects in mice. With the aid of osteoinductive materials, stem cells and/or osteoprogenitor cells migrating from the surrounding tissue into critical-sized defect sites are able to differentiate into bone-forming cells and regenerate bone.[36] CNT was not used in the animal study because CNT cannot be engineered into 3D scaffolds. Instead, as a comparative group, 3D scaffolds of non-osteoinductive poly(L-lactic acid) (PLLA), the accepted gold-standard material for scaffold, were prepared with electrospinning and lyophilization process in similar dimensions to the 3D cPAN scaffolds (Supporting Information, Figure S7) and implanted in vivo. The 3D PLLA scaffolds show comparable compressive modulus, surface area, and porosity to those of cPAN 3D scaffolds (Supporting Information, Table S1). The osteogenic efficacy of cPAN scaffolds loaded with bone morphogenetic protein 2 (BMP-2), an osteoinductive protein,[37] was also evaluated to examine the synergistic effects of cPAN and BMP-2 on bone formation. We hypothesized that the π electron clouds of cPAN would interact with the hydrophobic amino acids residues of BMP-2 through hydrophobic π–π stacking,[38] enabling the cPAN materials to synergistically act as both a drug delivery device and an osteoinductive scaffold. BMP-2 release from 3D cPAN scaffolds was evaluated by an enzyme-linked immunosorbent assay (ELISA). cPAN exhibited sustained in vitro release of BMP-2 up to 21 days, while PLLA showed an initial burst (80% release) of BMP-2 during the first 4 days (Figure 4A). This result demonstrated that cPAN can serve as a BMP-2 carrier as well as a 3D scaffold for bone regeneration.

To evaluate new bone formation by 3D cPAN scaffolds, the animals were sacrificed 8 weeks after scaffold implantation. Micro-computed tomography (micro-CT) results showed increased bone regeneration in the cPAN group compared to the PLLA group (Figure 4B). cPAN scaffold implantation stimulated bone regeneration that filled up to 52.7% of the original defect area, which was nearly 2.3-fold higher than the PLLA group. We observed higher extent of fibronectin adsorption on 3D cPAN scaffolds compared to the 3D PLLA scaffolds (Supporting Information, Figures S5, S8),

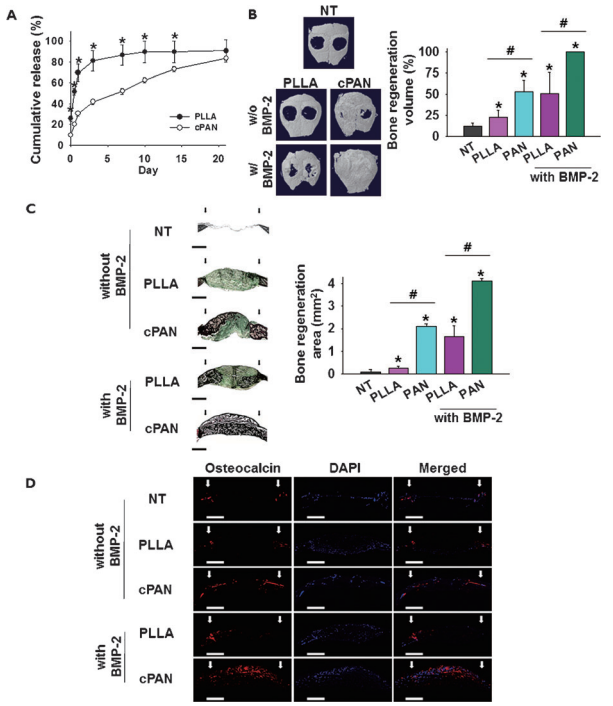

Figure 4. In vivo bone regeneration efficacy of 3D cPAN scaffolds with or without BMP-2 loading on scaffolds. The scaffolds were tested in a mouse calvarial defect model. The efficacy was compared to that of 3D electrospun PLLA scaffolds. A) Ability of cPAN to release BMP-2, an osteoinductive protein, in a sustained manner. ($n=3$, $^{*}P<0.05$ versus PLLA). B) In vivo bone regeneration of the calvarial defects. The regenerated bone volume was measured using a micro-CT analyzer program. The bone formation volume is presented as a percentage calculated from the ratio of newly formed mineralized bone volume over the initial defect volume. C) In vivo bone regeneration evaluated by histomorphometric analysis with Goldner's Trichrome staining of tissue specimens. The dark color indicates mineralized bone. The area of regenerated bone was determined using histomorphometry analysis. D) Immunohistochemical staining for osteocalcin (red). Cell nuclei were counter-stained with DAPI (blue). In (B) and (C), $n=4$, $^{*}P<0.05$ versus no treatment (NT) group, $^{\#}P<0.05$. In (C) and (D), the arrows indicate the calvarial defect margins; scale bars: 1 mm.

which contributes to the higher bone regeneration efficiency of 3D cPAN scaffolds. It has been reported that osteogenic differentiation of MSCs depends on the stiffness of the matrix.[39] However, the compressive modulus of 3D PLLA scaffolds and 3D cPAN scaffolds was not significantly different (Supporting Information, Table S1). Thus, the enhanced in vivo bone formation in the 3D cPAN scaffolds may be mainly caused by the higher adsorption of fibronectin (Supporting Information, Figures S5, S8) rather than the stiffness of the matrix. Remarkably, by loading a small amount (500 ng per implant) of BMP-2, all of the mice implanted with cPAN scaffolds showed complete bone regeneration. In contrast, mice with BMP-2 loaded PLLA scaffolds showed only 50.6% regeneration. This difference might be due to the sustained release of BMP-2 from cPAN scaffolds compared to the burst release from PLLA scaffolds (Figure 4A), as well as the osteoinductivity of cPAN (Figure 3). It is well-known that long-term release of BMP-2

enhances bone formation efficacy.[40] Moreover, despite the lower dose of BMP-2 used here (500 ng per implant) compared to previous studies on other BMP-2 carriers (1 μg[41,42] and 2.5 μg[43] per implant with the same volume), the combination of BMP-2 and cPAN was sufficient to achieve total bone defect regeneration. Histological analysis with Goldner's Trichrome staining and immunohistochemical staining of OC confirmed the micro-CT results and revealed more extensive bone formation in the cPAN scaffolds compared to the PLLA scaffolds with or without BMP-2, which substantiates the superior therapeutic efficacy of cPAN scaffolds for bone regeneration (Figure 4C and D). These in vivo data verify that the graphitic structure of cPAN not only acts as a direct osteogenesis-inducing factor but also serves as an effective drug delivery carrier.

In summary, the fabrication method in this work not only preserved the similarity of the chemical properties of cPAN to those of CNT but also allowed for control over the dimensions of cPAN scaffolds, which ultimately showed the potential of 3D cPAN scaffolds as a synthetic bone graft material. cPAN showed better biocompatibility compared to CNT and promoted mechanotransduction signaling of MSCs toward osteogenesis without the need for exogenous osteoinductive chemicals. The feasibility of using 3D cPAN scaffolds as a synthetic bone graft was also demonstrated in the animal study, with complete bone repair of critical-sized calvarial defects observed in mice implanted with BMP-2-loaded cPAN. While cPAN as a bioactive material has not been previously investigated, our study demonstrated the potential of cPAN for biomedical applications. The discovery of the unique bioactive properties of cPAN may lead to various applications for tissue engineering and regenerative medicine.

Received: March 28, 2014
Revised: May 31, 2014
Published online: July 7, 2014

Keywords: biological activity · carbon materials · mesenchymal stem cells · osteogenesis · polyacrylonitrile

[1] M. M. J. Treacy, T. W. Ebbesen, J. M. Gibson, *Nature* **1996**, *381*, 678 – 680.
[2] Y. Usui, K. Aoki, N. Narita, N. Murakami, I. Nakamura, K. Nakamura, N. Ishigaki, H. Yamazaki, H. Horiuchi, H. Kato, S. Taruta, Y. A. Kim, M. Endo, N. Saito, *Small* **2008**, *4*, 240 – 246.
[3] M. A. Correa-Duarte, N. Wagner, J. Rojas-Chapana, C. Morsczeck, M. Thie, M. Giersig, *Nano Lett.* **2004**, *4*, 2233 – 2236.
[4] S. W. Crowder, D. Prasai, R. Rath, D. A. Balikov, H. Bae, K. I. Bolotin, H. J. Sung, *Nanoscale* **2013**, *5*, 4171 – 4176.
[5] J. S. Lee, O. S. Kwon, S. J. Park, E. Y. Park, S. A. You, H. Yoon, J. Jang, *ACS Nano* **2011**, *5*, 7992 – 8001.
[6] J. S. Lee, O. S. Kwon, J. Jang, *J. Mater. Chem.* **2012**, *22*, 14565 – 14572.
[7] T. Kowalewski, N. V. Tsarevsky, K. Matyjaszewski, *J. Am. Chem. Soc.* **2002**, *124*, 10632 – 10633.
[8] W. X. Zhang, J. Liu, G. Wu, *Carbon* **2003**, *41*, 2805 – 2812.
[9] J. C. Chen, I. R. Harrison, *Carbon* **2002**, *40*, 25 – 45.
[10] C. Xu, R. Inai, M. Kotaki, S. Ramakrishna, *Tissue Eng.* **2004**, *10*, 1160 – 1168.
[11] S. Namgung, T. Kim, K. Y. Baik, M. Lee, J. M. Nam, S. Hong, *Small* **2011**, *7*, 56 – 61.
[12] S. Namgung, K. Y. Baik, J. Park, S. Hong, *ACS Nano* **2011**, *5*, 7383 – 7390.
[13] K. Y. Baik, S. Y. Park, K. Heo, K. B. Lee, S. Hong, *Small* **2011**, *7*, 741 – 745.
[14] R. McBeath, D. M. Pirone, C. M. Nelson, K. Bhadriraju, C. S. Chen, *Dev. Cell* **2004**, *6*, 483 – 495.
[15] P. S. Mathieu, E. G. Loboa, *Tissue Eng. Part B* **2012**, *18*, 436 – 444.
[16] J. S. Lee, O. S. Kwon, D. H. Shin, J. Jang, *J. Mater. Chem. A* **2013**, *1*, 9099 – 9106.
[17] Y. H. Lee, J. H. Lee, I. G. An, C. Kim, D. S. Lee, Y. K. Lee, J. D. Nam, *Biomaterials* **2005**, *26*, 3165 – 3172.
[18] L. Qiu, J. Z. Liu, S. L. Y. Chang, Y. Z. Wu, D. Li, *Nat. Commun.* **2012**, *3*, 1241.
[19] S. Deville, *Adv. Eng. Mater.* **2008**, *10*, 155 – 169.
[20] H. P. Yuan, C. A. Van Blitterswijk, K. De Groot, J. D. De Bruijn, *Tissue Eng.* **2006**, *12*, 1607 – 1615.
[21] C. M. Murphy, M. G. Haugh, F. J. O'Brien, *Biomaterials* **2010**, *31*, 461 – 466.
[22] J. P. McGann, M. J. Zhong, E. K. Kim, S. Natesakhawat, M. Jaroniec, J. F. Whitacre, K. Matyjaszewski, T. Kowalewski, *Macromol. Chem. Phys.* **2012**, *213*, 1078 – 1090.
[23] X. M. Li, H. F. Liu, X. F. Niu, B. Yu, Y. B. Fan, Q. L. Feng, F. Z. Cui, F. Watari, *Biomaterials* **2012**, *33*, 4818 – 4827.
[24] G. Raffaini, F. Ganazzoli, *Langmuir* **2004**, *20*, 3371 – 3378.
[25] K. A. Kilian, B. Bugarija, B. T. Lahn, M. Mrksich, *Proc. Natl. Acad. Sci. USA* **2010**, *107*, 4872 – 4877.
[26] J. Settleman, *Mol. Cell* **2004**, *14*, 148 – 150.
[27] M. F. Pittenger, A. M. Mackay, S. C. Beck, R. K. Jaiswal, R. Douglas, J. D. Mosca, M. A. Moorman, D. W. Simonetti, S. Craig, D. R. Marshak, *Science* **1999**, *284*, 143 – 147.
[28] A. K. Gaharwar, S. M. Mihaila, A. Swami, A. Patel, S. Sant, R. L. Reis, A. P. Marques, M. E. Gomes, A. Khademhosseini, *Adv. Mater.* **2013**, *25*, 3329 – 3336.
[29] P. Ducy, R. Zhang, V. Geoffroy, A. L. Ridall, G. Karsenty, *Cell* **1997**, *89*, 747 – 754.
[30] T. D. Ross, B. G. Coon, S. Yun, N. Baeyens, K. Tanaka, M. Ouyang, M. A. Schwartz, *Curr. Opin. Cell Biol.* **2013**, *25*, 613 – 618.
[31] A. R. Asthagiri, C. M. Nelson, A. F. Horwitz, D. A. Lauffenburger, *J. Biol. Chem.* **1999**, *274*, 27119 – 27127.
[32] B. G. Keselowsky, A. J. Garcia, *Biomaterials* **2005**, *26*, 413 – 418.
[33] J. Park, S. Park, S. Ryu, S. H. Bhang, J. Kim, J.-K. Yoon, Y. H. Park, S.-P. Cho, S. Lee, B. H. Hong, B.-S. Kim, *Adv. Healthcare Mater.* **2014**, *3*, 176 – 181.
[34] R. M. Salasznyk, R. F. Klees, W. A. Williams, A. Boskey, G. E. Plopper, *Exp. Cell Res.* **2007**, *313*, 22 – 37.
[35] M. A. Wozniak, C. S. Chen, *Nat. Rev. Mol. Cell Biol.* **2009**, *10*, 34 – 43.
[36] E. M. Bueno, J. Glowacki, *Nat. Rev. Rheumatol.* **2009**, *5*, 685 – 697.
[37] A. H. Reddi, *Nat. Biotechnol.* **1998**, *16*, 247 – 252.
[38] T. Utesch, G. Daminelli, M. A. Mroginski, *Langmuir* **2011**, *27*, 13144 – 13153.
[39] A. J. Engler, S. Sen, H. L. Sweeney, D. E. Discher, *Cell* **2006**, *126*, 677 – 689.
[40] W. G. La, S. Park, H. H. Yoon, G. J. Jeong, T. J. Lee, S. H. Bhang, J. Y. Han, K. Char, B. S. Kim, *Small* **2013**, *9*, 4051 – 4060.
[41] H. S. Yang, W. G. La, S. H. Bhang, T. J. Lee, M. Lee, B. S. Kim, *Tissue Eng. Part A* **2011**, *17*, 2153 – 2164.
[42] W. G. La, S. W. Kang, H. S. Yang, S. H. Bhang, S. H. Lee, J. H. Park, B. S. Kim, *Artif. Organs* **2010**, *34*, 1150 – 1153.
[43] K. Tachi, M. Takami, H. Sato, A. Mochizuki, B. H. Zhao, Y. Miyamoto, H. Tsukasaki, T. Inoue, S. Shintani, T. Koike, Y. Honda, O. Suzuki, K. Baba, R. Kamijo, *Tissue Eng. Part A* **2011**, *17*, 597 – 606.

